Optical properties of a single type of optically active center in Si/Si:Er nanostructures

N. Q. Vinh
Van der Waals-Zeeman Institute, University of Amsterdam, Valckenierstraat 65, NL-1018 XE Amsterdam, The Netherlands

H. Przybylińska
Institute of Physics, Polish Academy of Sciences, Al. Lotników 32/46, PL-02 668 Warszawa, Poland

Z. F. Krasil'nik
Institute for Physics of Microstructures, GSP-105, 603600 Nizhny Novgorod, Russia

T. Gregorkiewicz
Van der Waals-Zeeman Institute, University of Amsterdam, Valckenierstraat 65, NL-1018 XE Amsterdam, The Netherlands
(Received 12 May 2004; published 29 September 2004)

We present the results of high-resolution photoluminescence and magneto-optical spectroscopy of selectively doped Si/Si:Er nanolayer structures grown by sublimation molecular beam epitaxy method. We show that the annealing of such samples results in a preferential formation of a single type of optically active Er-related center. Detailed information on the microscopic structure of this center has been revealed from the investigation of the Zeeman effect. Its symmetry is found to be orthorhombic *I* (C_{2v}) and several *g*-tensors of the ground and excited states are determined. The consequences of current findings for the microscopic model of the Er-related center preferentially generated in Si/Si:Er nanolayers are discussed.

DOI: 10.1103/PhysRevB.70.115332 PACS number(s): 71.70.Ej, 78.66.Db, 61.72.Tt

I. INTRODUCTION

The optical properties of rare-earth (RE) atoms in semiconductors are the subject of a considerable amount of research due to the potential applications in optoelectronics.[1–5] The large interest in this field is motivated by the fact that these ions exhibit sharp, atomic-like, intra-4*f* optical transitions with temperature-independent wavelengths. Optical excitation of RE ions incorporated into glasses and ceramic materials is commonly used for lasers and optical amplifiers. In contrast to insulators, the major advantage of placing a RE ion in a semiconductor matrix is the possibility to excite its intra-4*f* transition electrically through a carrier-mediated process. In particular, erbium-doped silicon has attracted much attention. This is for two main reasons. First, the transition of the erbium ion from the first excited state to the ground state is in the 1.5 μm range which coincides with the optical window of glass fibers currently used for telecommunications. Second, this system can be easily integrated with devices manufactured using the highly successful standard silicon technology. Also, Si:Er light emitting structures are attractive in association with potential applications for optical interconnects in future photonic chip technology. As a result of a continuing research effort Si:Er-based light emitting diodes have now been successfully developed—for an up-to-date review, see, e.g., Refs. 6 and 7.

Unlike the well-investigated Yb in InP, Er^{3+} ion in a semiconductor matrix tends to form a variety of centers, resulting in multiplicity of photoluminescence (PL) spectra and, consequently, inhomogeneous broadening of emission lines. GaAs:Er prepared by ion implantation or by molecular beam epitaxy (MBE) exhibits a broad emission band around $\lambda = 1.5$ μm indicating simultaneous generation of several Er-related centers rather than formation of a single center with a well-defined structure.[8] A preferential production of one of the centers, however, was obtained for GaAs:Er by adjusting the MBE growth parameters. Zeeman effect[9] and PL excitation[10] studies revealed low-symmetry of this Er-related center. Selective development of a different Er-related center in GaAs was reported upon co-doping with oxygen in the ambient during the MOCVD growth. Also in this case, the spectral linewidth was sufficiently narrow to allow for structural investigations, and an ErO_2 cluster was proposed as a microscopic model for the relevant optical center.[11] This model was further corroborated by observation and analysis of the Zeeman effect.[12,13]

In contrast to GaAs:Er, very little is known on the microscopic structure of Er^{3+}- related optically active centers in silicon. This is very unfortunate, when bearing in mind the prominent position of Si:Er with respect to applications. Some information on microscopic structure of centers responsible for Er-related 1.5 μm emission in Si was revealed by a high-resolution PL study which identified more than 100 emission lines.[14] These were assigned to several, simultaneously present Er-related centers. In contrast to GaAs:Er, and also to GaN:Er, individual centers in Si:Er cannot be separated by excitation spectroscopy. The microscopic structure was investigated also using extended x-ray-absorption fine structure (EXAFS), and the presence of oxygen in the immediate surrounding of the optically active Er atom was concluded.[15] Formation of an Er-related cubic center was found in channeling experiments,[16] which identified an isolated Er ion at a tetrahedral interstitial site as the main center generated in crystalline silicon by Er implantation. This finding was in agreement with theoretical calculations predicting tetrahedral interstitial location of an isolated Er in Si.[17,18] Unfortunately, neither channeling experiments nor total energy calculations have shown whether the identified high-

symmetry Er centers are responsible for the emission observed in PL measurements. Also electron paramagnetic resonance (EPR), the experimental technique commonly applied to identify the microstructure of defects, has not been, so far, particularly successful in the case of the optically active Er-related centers in crystalline silicon.[19]

Structural information on optically active centers could be provided by magneto-optical studies. Unfortunately, in spite of numerous attempts, no successful observation of Zeeman effect in PL has been reported for Si:Er. Due to the aforementioned inhomogeneous character of the linewidth, application of magnetic field results in broadening and subsequent vanishing of emission lines. Realization of preferential formation of a single type of optically active Er-related centers is decisive for the future of Si:Er as photonic material. This goal is not achieved in "standard" Si:Er materials prepared by ion implantation, where a large variety of Er-related optically active centers are simultaneously generated.[14,20] Recently, we have confirmed[21] that the preferential production of a single type of optically active Er-related centers can be realized in Er-doped Si nanolayers grown by sublimation MBE (SMBE).[22] Using this technique, a sandwich structure of interchanged Si/Si:Er nanolayers can be grown. In this case, a high concentration of a specific center (labeled Er-1) was found. One can expect that in SMBE-grown multilayer structures of alternating Si and Si:Er layers,[22] conditions necessary for realization of efficient PL, i.e., high Er^{3+} ions concentration and efficient exciton generation, can be met simultaneously. Upon illumination with a laser beam, excitons generated in undoped Si spacer regions diffuse into doped layers and provide excitation of Er^{3+} ions. Moreover, we have established that spectral characteristics of emission related to the Er-1 center indicate a possibility $\sim 10^3$ higher value of absorption cross section, when compared to the implanted Si:Er materials used so far. Therefore the Er-1 center emerges as a plausible candidate for realization of optical gain in Si:Er.

In this paper we present an investigation of the Zeeman effect of the Er-1 center—the first Er-related optical center which can be preferentially produced in silicon. Highlights of the preliminary analysis of results of this study have been published before in Ref. 21.

II. SAMPLE PREPARATION AND EXPERIMENT

The SMBE method is a modification of MBE, in which fluxes of Si and dopants are produced by sublimation of appropriate current-heated sources.[23] SMBE allows us to grow both uniformly and selectively doped Si:Er structures with a minimum number of defects and a high concentration of dopants. We investigate here a novel type of selectively doped Si/Si:Er/Si/Si:Er/$\cdots$/Si multilayer structures of thin (δ) Si:Er layers alternating with Si spacers. The extraordinary properties of this material and, in particular, the strong enhancement of PL will be discussed.

The Si:Er layers used in this study were grown by SMBE on Si(100) *p*-type substrates ($\rho \approx 10-20\ \Omega$ cm) under pressure of 2×10^{-7} mbar. The growth temperatures (T_{gr}) were 430–700 °C. The PL intensity in a uniformly doped SMBE layer (a single layer) is most intense at a growth temperature of about 560 °C. To grow Er-doped silicon layers, polycrystalline Si plates intentionally doped with Er were used as a source for both Er and Si fluxes. The growth rate was varied from 0.3 to 5 μm/h and uniformly doped Si:Er layers with a thickness from 0.2 to 6 μm were obtained. For the selectively doped Si/Si:Er/Si/Si:Er/$\cdots$/Si multilayer structures, a thickness of Er-doped Si layers, $d_{Si:Er}$, was 2.0–50 nm, the thickness of Si space layers, d_{Si}, was 1.7–100 nm and the number of periods was $N=16-400$. Following the SMBE growth procedure, an additional annealing of the structures was carried out in a nitrogen or hydrogen flow at 800 °C for 30 min.[22] Table I shows the list of samples used in this research. For comparison, an implanted sample (labeled J900) has been added. This sample has been prepared by Er (energy 320 keV, dose 3×10^{12} cm^{-2}) and O (energy 40 keV, dose 3×10^{13} cm^{-2}) implantations followed by 900 °C/30 min anneal in nitrogen.

TABLE I. Sample labels, sample parameters, and annealing treaments for the investigated samples.

Sample label	$d_{Si:Er}$ (nm)	d_{Si} (nm)	N	ΣdSi:Er (μm)	$I_{Si:Er}$ (normalized)
#51	2.3	1.7	400	0.92	6.6
#52	2.3	6.5	196	0.45	11.4
#53	50	50	16	0.80	6.8
#54	6.2	31.3	44	0.27	30.5
#56	5.0	100	19	0.095	49.3
#37	1800		1	1.8	2.9
J 900	200		1	0.2	1

In the experiments, samples were excited using a cw argon-ion laser operating at 514.5 nm or 488 nm. All spectra were obtained with either a 1.0 m or 1.5 m F/8 monochromator (Jobin-Yvon THR-1000/THR-1500 equipped with a 900 grooves/mm grating blazed at 1.5 μm) and detected by a high sensitivity germanium detector (Edinburgh Instruments). Optical measurements were performed using a variable temperature continuous flow cryostat accessing the 1.5–300 K range (Oxford Instruments Optistat CF). For the Zeeman experiments, the sample was placed in a split-coil superconducting magnet with optical access (Spectromag 8). The magnetic field was varied from 0 up to 6 T.

III. PHOTOLUMINESCENCE

Figure 1 compares the 6500 cm^{-1} Er-related emission band from a "standard" J900 sample prepared by ion implantation (trace a) with that observed in the SMBE grown samples (traces b, c, d).

We used a uniformly doped SMBE sample (#37) with the highest total intensity of the integrated PL signal, a selectively doped SMBE sample (#51), and the sample #51 following a short annealing. The measurements were taken at 4.2 K, under identical conditions for all the samples. We point out that the preparation conditions of the ion-implanted sample were optimized in such a way as to obtain maximal

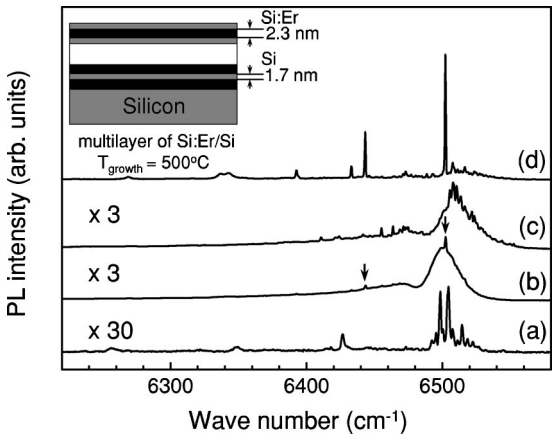

FIG. 1. PL spectra of a Si:Er sample prepared by implantation (a), the uniformly doped SMBE layer grown at 560°C (b), the selectively doped SMBE as grown at 500°C (c), and following a short annealing at 800°C for 30 min (d). All the spectra have been recorded at 4.2 K under Ar^+-ion laser excitation. In the inset, the multilayer structure of the SMBE grown sample is schematically illustrated.

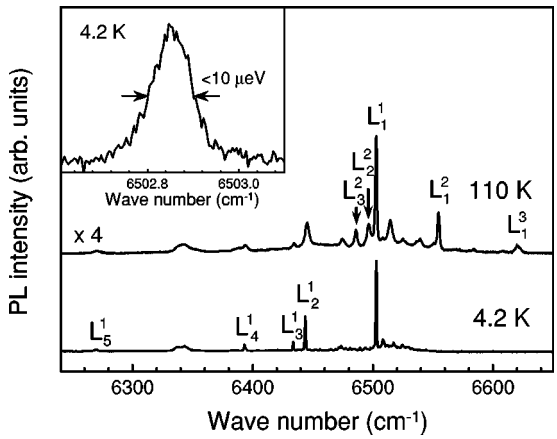

FIG. 2. PL spectra of the annealed #51 sample as measured at 4.2 and 110 K. For line positions, symbols, and halfwidths, see Table I. The inset shows a high-resolution scan of the most intense, L_1^1 line, of the Er-1 spectrum.

PL signal.[20] Nevertheless, the Si:Er layers grown by the SMBE method show stronger emission.

The PL spectrum of the uniformly doped SMBE layer is shown in Fig. 1, trace b. As can be seen, the PL intensity obtained in the SMBE grown sample (#37) exceeds considerably that of the ion implanted one. A broad spectral band is seen around the energy of 6506 cm^{-1} with the width about 25 cm^{-1}. It was suggested to originate from Er complexes of the so-called SiO_2-precipitate type center.[20] Along with the precipitate center, also the PL spectrum of the Er-1 center (marked by arrows in Fig. 1) can be distinguished. This spectrum has been reported before[22] and assigned to a low-symmetry Er-related center.

The sample #51 consists of 400 Si:Er layers of 2.7 nm thickness interlaced by 1.7 nm Si spacers. The structure is schematically depicted in the inset to Fig. 1. The PL spectrum of the as grown sample #51 is presented in Fig. 1, trace c. It has high intensity and shows multiple sharp features superimposed on a relatively broad band.

Detailed investigations revealed that at low temperature, the integrated intensity of the Er-related PL in optimized multilayer structures can be an order of magnitude higher than from a single Si:Er layer of an equal Er-doped volume. The intensity increase was found to depend strongly on the thickness and number of the undoped Si spacer layers. Table I lists the structure parameters for several of the investigated samples together with the integrated PL intensity ($I_{Si:Er}$) normalized for the same volume of Er doped layers and scaled with respect to the implanted sample. This is obtained by dividing the PL intensity over the total thickness $\Sigma d_{Si:Er}$ and the intensity of J900. It can be seen that $I_{Si:Er}$ increases with increasing thickness of the spacer layer up to 50 nm, at which point it exceeds the $I_{Si:Er}$ intensity of the uniformly doped Si:Er layer by more than an order of magnitude. The enhancement of the luminescence intensity in the multilayer structures as compared to uniformly doped layers may be related to more efficient Er excitation. As known, the maximum values for quantum efficiency and PL intensity in Si:Er structure are reached at low temperatures when excitation of Er^{3+} occurs through of an intermediate state with participation of an exciton. One may speculate that in a multilayer structure, excitons efficiently generated in Si spaces have long lifetime and can subsequently diffuse towards Er doped regions. In that way they provide an excitation additional to that by excitons induced in the Si:Er layer.

Annealing considerably alters PL characteristics of the multilayer structure—see trace d in Fig. 1. While the total intensity of emission changes only slightly, the spectrum undergoes an important transformation: the broad band disappears and a small number of sharp and intense lines of the Er-1 PL spectrum remain. This is illustrated in Fig. 2, for measurements taken at 4.2 and 110 K. The inset shows a high-resolution scan of the main feature of the Er-1 spectrum. As can be seen, the real width of this PL line is measured to be extremely small $\Delta E \leqslant 0.08$ cm^{-1} (10 μeV). To our best knowledge, this is among the smallest values ever measured for any emission band in a semiconductor matrix. At low temperature, below 25 K, the Er-1 spectrum consists of a set of narrow intense lines at energies of 6502.85, 6443.72, 6433.59, 6393.17 cm^{-1}. For further reference we label these line 1 (L_1^1), line 2 (L_2^1), line 3 (L_3^1), and line 4 (L_4^1), respectively. At higher temperatures other lines, labeled hot line 1 (L_1^2), hot line 2 (L_2^2), hot line 3 (L_3^2), and a second hot line 1 (L_1^3), appear at 6554.82, 6496.03, 6485.65, and 6620.97 cm^{-1}, respectively. The intensities of these lines rapidly increase with increasing temperature while, at the same time, the intensities of the lines L_1^1, L_2^1, L_3^1, L_4^1 decrease. These details of the spectra are presented in Table II. We note that the hot lines are displaced by about 52 cm^{-1}.

Temperature dependence of luminescence has been investigated in more detail in order to determine the electronic level scheme of the optically active center responsible for the Er-1 spectrum. The temperature was varied between 4.2 K and 160 K. The intensity ratios of the lines L_1^2, L_2^2, L_3^2 to that of L_1^1, L_2^1, L_3^1, obtained from the measurements, are plotted as a function of temperature in Fig. 3 (traces c, b, and a, respec-

TABLE II. Labeling and spectroscopic parameters of the Er-related photoluminescence lines.

Transition	Label	$h\nu$(cm^{-1})	Displacement (cm^{-1})
Line 1	L_1^1	6502.85	
Line 2	L_2^1	6443.72	−59.13 from L_1^1
Line 3	L_3^1	6433.59	−69.26 from L_1^1
Line 4	L_4^1	6393.17	−109.68 from L_1^1
Line 5	L_5^1	6269.96	−232.89 from L_1^1
Hot line 1	L_1^2	6554.82	51.97 from L_1^1
Hot line 2	L_2^2	6496.03	52.31 from L_2^1
Hot line 3	L_3^2	6485.65	52.06 from L_3^1
Second hot line 1	L_1^3	6620.97	66.51 from L_1^2

tively). From the Arrhenius plot, we conclude the same activation energy of 49 ± 3 cm^{-1} for all of them. This value is in good agreement with separation of lines L_1^2, L_2^2, L_3^2 to the lines L_1^1, L_2^1, L_3^1, (51.97, 52.31, 52.06 cm^{-1}, respectively). Also, the intensity ratio of the lines L_1^3 to that of L_1^2 has an activation energy of 72 ± 8 cm^{-1} (trace d), very similar to the spectroscopic splitting of L_1^3 and L_1^2, (66.51 cm^{-1}).

Based on the PL investigation we can interpret the observed structure of the spectrum at low temperature as transitions from the lowest excited state to the crystal field split ground state. At elevated temperatures satellites of these lines can be detected, as shown in Fig. 2. They are shifted by 52 and 118 cm^{-1} (6.4 and 14.6 meV) towards higher energies for each transition, and can be associated with transitions originating at the second and the third crystal field split levels of the excited state. Such an energy level diagram responsible for PL of the Er-1 center is shown in the inset to Fig. 3.

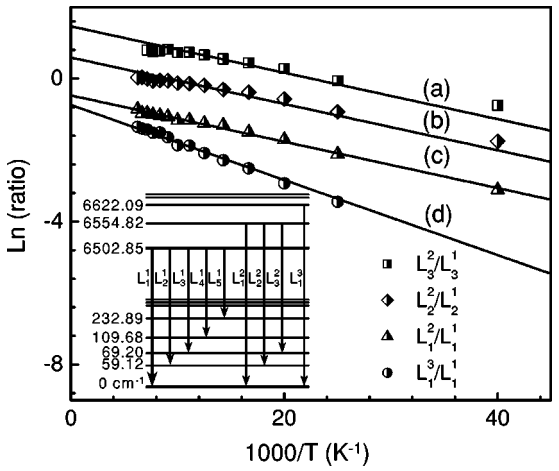

FIG. 3. Arrhenius plots of the temperature variation of the intensity ratios of the hot line 1 (L_1^2) relative to the line 1 (L_1^1) (triangles); the hot line of line 2 (L_2^2) relative to the line 2 (L_2^1) (diamonds); the hot line of line 3 (L_3^2) relative to the line 3 (L_3^1) (squares). The activation energies are found to be $\Delta E \simeq 50$ cm^{-1}, equal to the spectroscopic splitting. The intensity ratio of the second hot line L_1^3 relative to line 1 (L_1^1) (circles) is shown as trace d; it has an activation energy of 72 ± 8 cm^{-1}, equal to the L_1^3 to L_1^2 energy separation.

IV. ZEEMAN SPLITTING OF THE PL LINES

A. Introduction: theoretical considerations

The electronic configuration of Er^{3+} is 4 f^{11} with a ground state $^4I_{15/2}$ and a first excited state $^4I_{13/2}$. In a crystal field with T_d symmetry the ground state $^4I_{15/2}$ will split into two doublets, Γ_6 and Γ_7, and three Γ_8 quadruplets, whereas the first excited state ($^4I_{13/2}$) splits into $2\Gamma_6+\Gamma_7+2\Gamma_8$. This splitting is described by the crystal field Hamiltonian[24]

$$\mathcal{H} = B_4(O_4^0 + 5O_4^4) + B_6(O_6^0 - 21O_6^4), \tag{1}$$

where O_l^m are Steven's equivalent operators and the B_l are adjustable parameters related to the strength of the crystal field components. Alternatively, the Hamiltonian can be expressed in the notation introduced by Lea, Leask, and Wolf (LLW),[25,26]

$$\mathcal{H} = \frac{Wx}{F(4)}(O_4^0 + 5O_4^4) + \frac{W(1-|x|)}{F(6)}(O_6^0 - 21O_6^4). \tag{2}$$

The parameters W and x are related to B_4 and B_6 as $B_4F(4)=Wx$, $B_6F(6)=W(1-|x|)$. W is an energy scale factor. The dimensionless parameter x can take values from 0 to ±1, which covers the range of the B_4/B_6 ratios between 0 and ±∞. Negative values of x correspond to tetrahedral coordination, whereas positive values of x occur for octahedral coordination. The factors $F(4)$ and $F(6)$ are introduced to keep the eigenvalues in the same numerical range for all ratios of the fourth to sixth degree terms. For $J=15/2$, $F(4)=60$, $F(6)=13860$ and for $J=13/2$, they are 60 and 7560, respectively.[25] In Fig. 4 we reproduce the LLW calculations of the eigenvalues for $J=15/2$ and $J=13/2$. The state labeling is that for T_d symmetry.[27] Note that all matrix elements, and hence all eigenvalues, are proportional to W; in Fig. 4 they are presented with the energy scale parameter set to $W=1$ cm^{-1}, and are functions of x only.

The eigenfunctions expressed in the basic states $|M_J\rangle$ are either of the form

$$|\psi_1, \mp\rangle = \mp\left(a_1\left|\pm\tfrac{15}{2}\right\rangle + a_2\left|\pm\tfrac{7}{2}\right\rangle + a_3\left|\mp\tfrac{1}{2}\right\rangle + a_4\left|\mp\tfrac{9}{2}\right\rangle\right) \tag{3a}$$

for $J=15/2$, and

$$|\psi_2, \mp\rangle = \mp\left(b_1\left|\pm\tfrac{7}{2}\right\rangle + b_2\left|\mp\tfrac{1}{2}\right\rangle + b_3\left|\mp\tfrac{9}{2}\right\rangle\right) \tag{3b}$$

for $J=13/2$, or

$$|\psi_3, \mp\rangle = \mp\left(c_1\left|\pm\tfrac{13}{2}\right\rangle + c_2\left|\pm\tfrac{5}{2}\right\rangle + c_3\left|\mp\tfrac{3}{2}\right\rangle + c_4\left|\mp\tfrac{11}{2}\right\rangle\right) \tag{4}$$

for both $J=15/2$ and 13/2. In an external magnetic field the degeneracy of the crystal-field split levels is lifted. The splitting of the doublet states can be described by an effective spin $\tilde{S}=1/2$ and labeling of the state $|\mp\rangle$. If the Zeeman interaction is much smaller than the crystal field splitting, the Zeeman interaction has the form

$$\mathcal{H} = g\mu_B \mathbf{B}\cdot\tilde{\mathbf{S}}, \tag{5}$$

where μ_B being the Bohr magneton, and g the effective g-value.

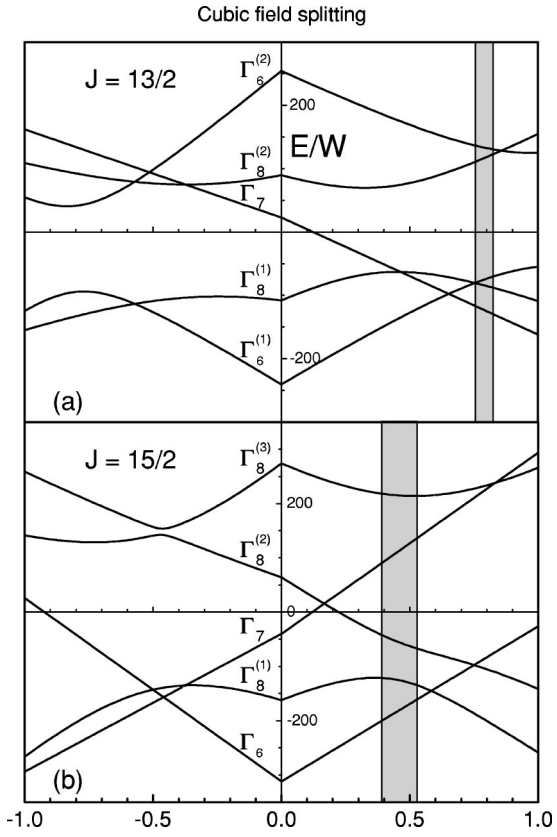

FIG. 4. The energy-level splitting of a $J=15/2$ (a) and a $J=13/2$ (b) manifold by a cubic crystal field of T_d symmetry Ref. 25. Possible locations of the ground and the first excited states of the Er-1 center are indicated.

The coefficients in Eqs. (3a) and (3b) can be uniquely determined for the Γ_7 doublets and those in Eq. (4) for the Γ_6 doublet. The effective g-factors of these states can be easily calculated ($g=2g_J\Sigma_{M_J}a_J^2M_J$, where g_J is the Landé factor). The Landé g-factor of the free Er^{3+} ions is $g_J=\frac{6}{5}$ for the pure ground state $^4I_{15/2}$, and $g_J=\frac{72}{65}$ for the pure first excited state $^4I_{13/2}$. In T_d symmetry the (isotropic) effective g-factors are thus 6.80 and 6.00 for the Γ_6 and Γ_7 symmetry doublets, respectively, of a pure $^4I_{15/2}$ manifold, while for the Γ_7 doublet of the $^4I_{13/2}$ multiplet $g=5.54$. For all the other states the coefficients in the wave functions, and hence the effective g-factors, depend on crystal field parameters.

The quadruplets Γ_8 can be described by an effective spin of $\tilde{S}=3/2$, where the $M_{\tilde{S}}=\mp\frac{1}{2}$ states have the form given by Eqs. (3a) and (3b) and the $M_{\tilde{S}}=\mp\frac{3}{2}$ states have the form given by Eq. (4). The Zeeman interaction for a Γ_8 quadruplet is more complicated than that for the ordinary $J=3/2$ quadruplet, as there are nonvanishing matrix elements between the $M_{\tilde{S}}=\mp\frac{3}{2}$ wave functions. The Hamiltonian describing the Zeeman interaction within a Γ_8 quadruplet can be expressed by[28]

$$\mathcal{H}=g_J\mu_B(a\mathbf{B}\cdot\tilde{\mathbf{S}}+b(B_x\tilde{S}_x^3+B_y\tilde{S}_y^3+B_z\tilde{S}_x^3)). \tag{6}$$

The parameters a and b can be expressed also as $a=-P/12+9Q/4$, $b=P/3-Q$, where P and Q are the expectation values of $(a\mathbf{B}\cdot\tilde{\mathbf{S}}+b(B_x\tilde{S}_x^3+B_y\tilde{S}_y^3+B_z\tilde{S}_x^3))$ for $|+\frac{3}{2}\rangle$ and $|+\frac{1}{2}\rangle$ states, respectively. In an ordinary $J=3/2$ quadruplet $P=3Q$ and, in consequence, $b=0$.

TABLE III. The selection rules of the ED and MD transitions.

	$\Gamma_6\|+\rangle$	$\Gamma_6\|-\rangle$	$\Gamma_7\|+\rangle$	$\Gamma_7\|-\rangle$
$\Gamma_6\|+\rangle$	MD	MD	ED	0
$\Gamma_6\|-\rangle$	MD	MD	0	ED
$\Gamma_7\|+\rangle$	ED	0	MD	MD
$\Gamma_7\|-\rangle$	0	ED	MD	MD
$\Gamma_8\|+\frac{3}{2}\rangle$	MD+ED	MD+ED	MD+ED	0
$\Gamma_8\|+\frac{1}{2}\rangle$	MD+ED	0	MD+ED	MD+ED
$\Gamma_8\|-\frac{1}{2}\rangle$	0	MD+ED	MD+ED	MD+ED
$\Gamma_8\|-\frac{3}{2}\rangle$	MD+ED	MD+ED	0	MD+ED

In a free ion electric dipole (ED) transitions between the levels of the $4f^n$ configuration are parity forbidden and only magnetic dipole transitions (MD) are expected. However, the crystal field of the host material may break the inversion symmetry and admix states of opposite parity via odd terms in the crystal field potential, which makes ED transitions partly allowed. The selection rules governing optical transitions between Zeeman split levels of Er^{3+} are the following: MD transitions can occur between states of $\Delta J=0$, ±1, $\Delta M_J=0$, ±1, whereas ED transitions can occur between states with $\Delta J\leqslant6$, $\Delta M_J=0$, ±1. The T_d symmetry imposes further restrictions on the selection rules: transitions between two doublets of the same symmetry are only MD allowed, whereas those between Γ_6 and Γ_7 doublets are only ED allowed. Moreover, in the latter case only $|\pm\rangle\leftrightarrow|\pm\rangle$ transitions can occur. Transitions to and from a Γ_8 quadruplet are both ED and MD allowed.[29] The allowed transitions in pure T_d symmetry are summarized in Table III. According to these selection rules, for Er^{3+} in a site of T_d symmetry we should expect, assuming that the initial state is a doublet, the following number of Zeeman components: 2 for emission terminating on a doublet of the other symmetry, 4 for a doublet of the same symmetry, and 6 components for the emission terminating on either of the 3 quadruplets. We will refer to Table III frequently in the following sections, as it will turn out that the optical transitions of the Er center under investigation closely follow the selection rules for the cubic symmetry.

In a crystal field of lower than cubic symmetry the $^4I_{15/2}$ and $^4I_{13/2}$ will split into 8 and 7 Kramers' doublets, respectively. In particular, in an orthorhombic C_{2v} crystal field all the doublets would be of the same Γ_5 symmetry and optical transitions between them would be MD and ED allowed. The crystal field splitting is described by the following Hamiltonian:

$$\mathcal{H}=B_2^0O_2^0+B_2^2O_2^2+B_4^0O_4^0+B_4^2O_4^2+B_4^4O_4^4+B_6^0O_6^0+B_6^2O_6^2+B_6^4O_6^4+B_6^6O_6^6. \tag{7}$$

Here two of the quantization axes are oriented along non-

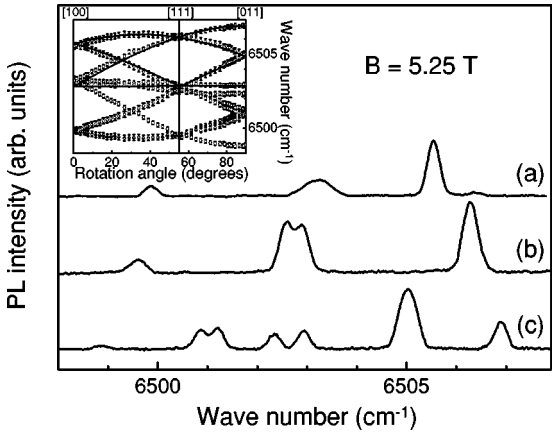

FIG. 5. Zeeman effect for the main PL line L_1^1 at 4.2 K for magnetic field of 5.25 T oriented along the main crystal directions (a) $\mathbf{B}||\langle 100\rangle$, (b) $\mathbf{B}||\langle 111\rangle$, and (c) $\mathbf{B}||\langle 011\rangle$. Inset to the figure: angular dependence of the Zeeman effect for the line L_1^1 at $B=5.25$ T for the (011) crystallographic plane.

equivalent $\langle 011\rangle$ directions perpendicular to each other, taken as x' and y', while the z' axis is the $\langle 100\rangle$ oriented intersection of the planes, perpendicular to x' and y'. The Zeeman interaction Hamiltonian for well separated doublets (where second order effects can be ignored) takes the form,

$$\mathcal{H} = \mu_B \mathbf{B}\cdot\mathbf{g}\cdot\tilde{\mathbf{S}}, \tag{8}$$

where $\mathbf{g}$ is now a tensor with the main axes oriented along x', y', and z'.

If the distortion of cubic symmetry is small, i.e., the splitting of the quadruplets is much smaller than the distance to the next "cubic" level, the influence of Hamiltonian (7) on a Γ_8 *quadruplet* can be expressed by the so-called quadrupole term, $\tilde{\mathbf{S}}\cdot\mathbf{D}\cdot\tilde{\mathbf{S}}$, which in the defect axes takes the form[24]

$$\mathcal{H} = D\left(\tilde{S}_{z'}^2 - \tfrac{1}{3}\tilde{S}(\tilde{S}+1)\right) + E(\tilde{S}_{x'}^2 - \tilde{S}_{y'}^2). \tag{9}$$

The total Hamiltonian, which needs to be considered is

$$\mathcal{H} = \mu_B g_J (a\mathbf{B}\cdot\tilde{\mathbf{S}} + b(B_x\tilde{S}_x^3 + B_y\tilde{S}_y^3 + B_z\tilde{S}_x^3)) + \tilde{\mathbf{S}}\cdot\mathbf{D}\cdot\tilde{\mathbf{S}}. \tag{10}$$

B. Splitting of line L_1^1

The Zeeman splitting of the main PL line L_1^1 measured at 4.2 K in magnetic field of 5.25 T is shown in Fig. 5. For the field oriented along the principal directions, three Zeeman components for $\mathbf{B}||\langle 100\rangle$, four components for $\mathbf{B}||\langle 111\rangle$ and seven components for $\mathbf{B}||\langle 011\rangle$ can be seen. The angular dependence of the line positions, measured at 5.25 T in the {011} crystal plane from [001] direction to [011], is depicted in the inset of Fig. 5. The clearly observed strong dependence of the Zeeman splitting on the orientation of the magnetic field indicates that the center has lower than cubic symmetry. The center has only four nonequivalent orientations for an arbitrary direction of $\mathbf{B}$ in this plane, with two orientations for $\mathbf{B}$ along $\langle 100\rangle$ and $\langle 111\rangle$ directions, and three for $\langle 001\rangle$ direction. This is a clear and unambiguous signature of orthorhombic I (C_{2v}) symmetry. As explained in detail in Ref. 21, the angular as well as the magnetic field dependencies can be only described with $g_x^{(1)}=G_x^{(1)}=0\pm 0.1$, $g_y^{(1)}-G_y^{(1)}=3.3\pm 0.1$, and $g_z^{(1)}=G_z^{(1)}=0\pm 0.1$, where $\mathbf{g}^{(1)}$ and $\mathbf{G}^{(1)}$ refer to g-tensor values for the $J=15/2$ and $J=13/2$ manifolds, respectively, and the superscript denotes the position of the level in the manifold. For sake of consistency we point out that in our preliminary analysis[21] a different tensor axes set was adopted, with the z axis chosen as the one with the only nonvanishing g-value. The solid lines in the inset to Fig. 5 show the peak positions calculated with use of Eq. (8) for $|\pm\rangle\leftrightarrow|\pm\rangle$ transitions, which were the only ones observed. Hence, the individual g-tensors of the upper and lower doublets $\mathbf{g}^{(1)}$ and $\mathbf{G}^{(1)}$ could not be determined. The values were estimated from the temperature dependence of the intensity ratio of the high and the low energy Zeeman components at high field, under assumption of full thermalization, to be $\mathbf{G}^{(1)}=[0\pm 0.1, 15.1\pm 0.8, 0\pm 0.1]$, which implied $\mathbf{g}^{(1)}=[0\pm 0.1, 18.4\pm 0.8, 0\pm 0.1]$.[21]

The g-tensor values $\mathbf{G}^{(1)}$ for the excited state can be determined with a better accuracy from the analysis of the Zeeman splitting of the line L_4^1, presented in the next subsection, of which transitions with the difference as well as the sum of the effective g-factors of the ground and excited states were observed. We will, therefore, defer the discussion of the determined g-tensor values until later. We would only like to point out at this stage that despite the anisotropy of the g-tensor determined here, the optical transitions remarkably resemble those expected between doublets of different type in T_d symmetry (Table III).

C. Splitting of line L_4^1

The Zeeman splitting of line L_4^1, as measured at 4.2 K for two orientations of the magnetic field $\mathbf{B}||\langle 100\rangle$ and $\mathbf{B}||\langle 011\rangle$, is shown in Figs. 6(a) and 6(b), respectively. For $\mathbf{B}$ oriented along the cube axis, $\mathbf{B}||\langle 100\rangle$, four dominant Zeeman components are observed. In addition, weaker Zeeman components originating from a relatively broad shoulder line partly superimposed on L_4^1 are seen. For $\mathbf{B}$ along $\langle 011\rangle$ up to 12 Zeeman components are seen at 5 T. The overall splitting is about an order of magnitude larger than that for L_1^1.[21] The effective g-factors for the outer Zeeman components are about 20 for both magnetic field orientations. We conclude that, unlike in the case of L_1^1, here we observe transitions not only with the difference, $(G-g)$, but also with the sum, $(G+g)$, of the effective g-factors of the excited and ground states.

By simulating the line positions with Hamiltonian (8) we can determine both the g-tensor values for the ground state, $\mathbf{g}^{(4)}=[8.3\pm 0.5, 7.6\pm 0.5, 1.6\pm 0.3]$, and the excited state, $\mathbf{G}^{(1)}=[0\pm 0.1, 14.8\pm 0.5, 0\pm 0.1]$. As can be seen from the solid lines in Fig. 6, the simulation gives in this case good agreement with the experimental data for all $(G-g)$ and $(G+g)$ transitions and all nonequivalent orientations in C_{2v} symmetry. Due to the fact that $G_z=0$, i.e., there is no Zeeman splitting in the excited state at $\mathbf{B}||\langle 100\rangle$ for the defect con-

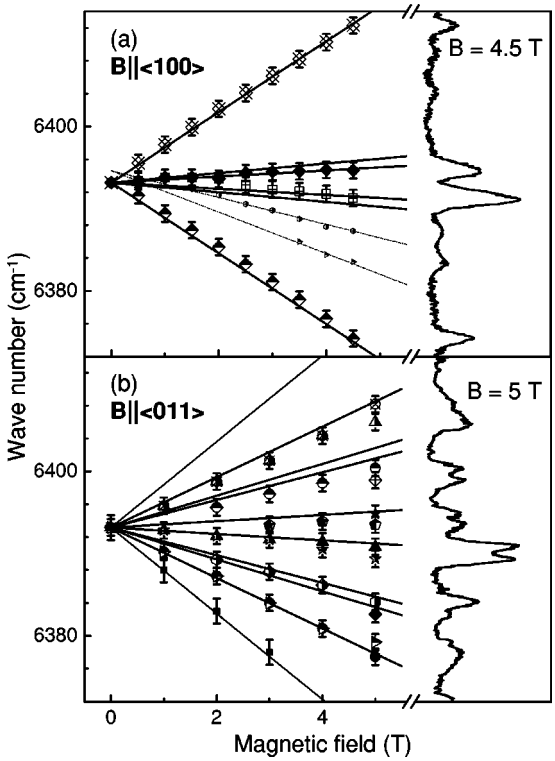

FIG. 6. Zeeman effect of the line L_4^1, with the magnetic field along the main crystal directions (a) $\mathbf{B}||\langle 100\rangle$, and (b) $\mathbf{B}||\langle 011\rangle$, at $T=4.2$ K.

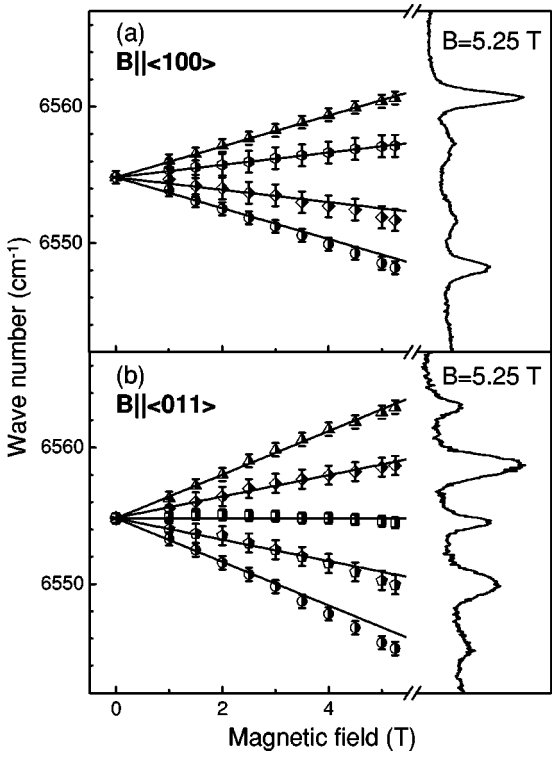

FIG. 7. Zeeman effect of the line L_1^2 (hot line of line L_1^1) with the magnetic field along the main crystal directions (a) $\mathbf{B}||\langle 100\rangle$, and (b) $\mathbf{B}||\langle 011\rangle$, at $T=55$ K.

figuration with **B** parallel to *z*, the $(G-g)$ and $(G+g)$ transitions coincide reducing the number of Zeeman components from four to two. For other defect configuration the energies are very close to those of the $(G-g)$ transitions, with the energy difference falling within the linewidth (indicated by error bars in Fig. 6). In contrast, the lines with the sum $(G+g)$ of the effective *g*-values can be seen. Hence, for $\mathbf{B}||\langle 100\rangle$ only four separated PL lines are observed.

Similarly, since $G_x=0$, for $\mathbf{B}||\langle 011\rangle$ ten out of twelve possible components are expected, with one being too weak to be detected. At high fields additional splitting for two configurations appears which indicates some misorientation of the rotation plane. The calculated line positions agree very well with the experimental ones within the whole magnetic field range studied only for the lower energy Zeeman components. The peak energies for the higher energy Zeeman components depend nonlinearly on *B* at higher fields, due to interaction with the second, close lying excited state.

The determined G_y tensor value for the excited state agrees within the experimental error with the value estimated in Ref. 21 from Zeeman splitting of L_1^1, but it is more accurate. We can now use this value to give the accurate tensor values for the ground state involved in L_1^1 $\mathbf{g}^{(1)}=[0\pm0.1, 18.1\pm0.5, 0\pm0.1]$

D. Splitting of line L_1^2 (the hot line)

The splitting of the hot line, labeled L_1^2 in Table II, in magnetic fields up to 5.25 T at 55 K is shown in Fig. 7. Five components are observed for $\mathbf{B}||\langle 011\rangle$ and four components are seen for $\mathbf{B}||\langle 100\rangle$. The pattern of the Zeeman splitting is very similar to that of line L_1^1 stemming from transitions between two doublets of ground and excited state. For line L_1^1 three components were seen with the field oriented along $\langle 100\rangle$ due to the fact that the g_z tensor values vanished for both the ground and the excited state, whereas the excited state involved in L_1^2 has a nonzero g_z value. The absolute magnitude of the splitting is also comparable. Moreover, just like in the case of line L_1^1, only transitions with a difference of the effective *g*-factors can be observed.

The splitting of line L_1^2 can be very well described with the following *g*-tensor for the second excited state: $|\mathbf{G}^{(2)}|=[0\pm0.1, 11.2\pm0.5, 2.0\pm0.2]$ (the *g*-tensor of the ground state being the same as for L_1^1). The simulation of line positions by Eq. (8) with these parameters is shown by solid lines in Fig. 7. The deviation from linear dependence observed for lower energy Zeeman components is due to the fact that at high magnetic fields the magnitudes of the Zeeman and the crystal field interactions become comparable, resulting in mixing between sublevels in the $J=15/2$ manifolds. The higher energy Zeeman components corresponding to transitions from the lower lying level of the excited state doublet to the lower lying level of the ground state doublet are less affected.

E. Splitting of other spectral components

The Zeeman effect was also investigated for the L_2^1 and L_3^1 PL lines. The experimental peak positions versus magnetic

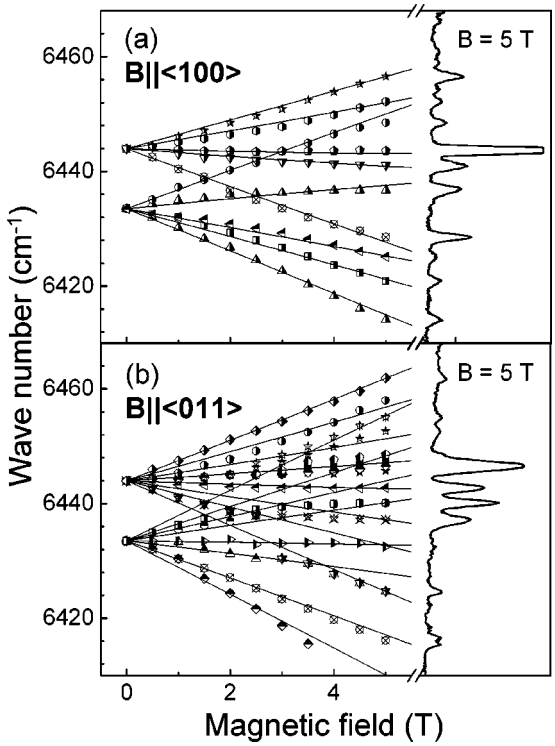

FIG. 8. Zeeman effect of the line L_2^1 and line L_3^1, with the magnetic field along the main crystal directions (a) $\mathbf{B}||\langle 100\rangle$, and (b) $\mathbf{B}||\langle 011\rangle$, at $T=4.2$ K.

field are shown in Fig. 8 for the $\mathbf{B}||\langle 100\rangle$ and $\mathbf{B}||\langle 011\rangle$ field directions. The Zeeman splitting pattern suggests that we deal in this case with transitions from the excited doublet state to a Γ_8 quadruplet split by a lower symmetry crystal field. We can speculate that if the low symmetry distortion is small, the selection rules valid for T_d symmetry may approximately hold at high magnetic fields, when the states could regain their initial "cubic" character. In other words, any extra Zeeman component in the PL to those determined by Tables III will have lower intensity. Based on that, we can predict the number of "strong" Zeeman components observed in the PL for a center with small C_{2v} distortion. For $\mathbf{B}||\langle 100\rangle$ we should see two nonequivalent defect configurations, one with $\mathbf{B}||z$ and one with $\mathbf{B}$ in the plane perpendicular to z. We should, hence, see six components for the latter but only four components for the former, as there is no splitting of the excited state in this configuration $[G_z^{(1)}=0]$. Similarly, for $\mathbf{B}||\langle 011\rangle$, with three nonequivalent defect configurations, we should see $6+6+4=16$ components. As illustrated by Fig. 8, this is exactly what we observed in the experiment.

The solid lines in the Fig. 8 are guide for eye only. In order to determine the parameters reliably, additional experiments are necessary, either at low magnetic fields—when the Zeeman interaction is much weaker than the crystal field splitting and doublets can be treated separately, or in the opposite regime—when the Zeeman splitting is much larger than the crystal field splitting.

We have also measured a magnetic induced splitting of line L_5^1 for $\mathbf{B}||\langle 001\rangle$. The splitting pattern is very similar to that observed for L_4^1, i.e., the dominant transitions are those with a sum and difference of the effective g-factors for the two coinciding configurations. Due to the low PL intensity, it was not possible to measure the splitting for $\mathbf{B}||\langle 011\rangle$; hence the g-tensor values could not be determined. All determined g-tensor values are listed in Table IV.

TABLE IV. g-tensor values used for the calculated splitting.

Line label	Initial state	G_{av}	Final state	g_{av}
L_1^1	0 14.8 0	5.0±0.5	0 18.1 0	6.1±0.5
L_1^2	0 11.2 2	4.4±0.5	0 18.1 0	6.1±0.5
L_4^1	0 14.8 0	5.0±0.5	8.3 7.6 1.6	5.8±0.5

V. DISCUSSION AND CONCLUSIONS

A. Symmetry consideration

On the basis of the experimental data reported here, the following picture can be proposed. The PL spectrum observed in SMBE grown samples is characterized by a small number of very narrow lines. Although sharp emission bands should be expected for Er in view of the very long radiative lifetime of its excited $^4I_{13/2}$ state (~ms), linewidths of several meV are routinely observed for Er-related optical centers in crystalline silicon. Therefore it appeared that in the present case emission bands are characterized by the truly homogeneous linewidth. This has indeed been confirmed by, and formed a necessary prerogative for, the successful observation of the Zeeman effect, as reported in the current study. From analysis of the Zeeman effect we conclude that all the major lines of the observed PL spectrum originate from the same center, the Er-1. Such a conclusion is also consistent with the thermally-induced changes of the PL spectrum, with all the major features—lines L_1^1 to L_4^1—developing hot lines with identical energy spacings, indicating the common excited state for their origin. In this way the current study unambiguously shows that a preferential formation of one specific type of Er-related optically active center is realized in annealed SMBE-grown multinanolayer structures.

From the analysis of the angular dependence of the magnetic field induced splitting of PL lines, the C_{2v} symmetry of the Er-1 center has been established, and individual g-tensors for several crystal field split levels within ground and excited state multiplets have been determined. These are summarized in Table IV.

Although the lower-than-cubic symmetry of the Er-1 center is concluded from experiment, the distortion from cubic symmetry appears to be small. This is evident from the fact that optical transitions follow the selection rules for T_d symmetry rather than those for transitions between Γ_5 states of C_{2v} symmetry, where all the transitions would have equal probability. We could speculate that the observed orthorhombic I symmetry could arise from a distortion of an tetrahedrally coordinated Er^{3+} ion.

If only a small distortion of cubic symmetry is present, the average g_{av} factor can be related to the isotropic cubic g_c factor by[32]

$$g_{av} = g_c = \tfrac{1}{3}(g_x + g_y + g_z). \quad (11)$$

In the case of line L_1^1 the average g_{av} value for the lowest level of the ground state is 6.1 ± 0.5, slightly smaller than 6.8 the value characteristic for pure Γ_6, and similar to values found for Er in different host materials.[19,27,30–33] Therefore the Er-1 center ground state is likely to be of the Γ_6 character. The g_{av} values of the initial and final states determined from all the investigated transitions are also shown in the Table IV.

For the lowest level of the first excited state, the g_{av}-value is determined as 4.9 ± 0.5. It is similar to the (isotropic) g-factor of the Γ_7 states of a pure $^4I_{13/2}$ manifold of 5.54. As can be seen from Table III, this indicates that for line L_1^1 we deal mostly with electric-dipole-type transitions, without spin flips. This is to be expected for Er, since the strong spin-orbit coupling, characteristic for rare-earth ions, leads to the admixture of different excited configurations. The g-values determined here are smaller than these found in more ionic hosts. This can be due to covalent effects, as the results of the Landé factor becomes smaller because of stronger quenching of the orbital momentum. The Zeeman splittings of lines L_2^1 and L_3^1 behave like a transition from a doublet to a distorted Γ_8 quadruplet. The splitting of line L_4^1 indicates a doublet to doublet transition. However in that case we can see PL lines corresponding to the sum and the difference of the g-tensors of the ground and the excited states. Also the hot line L_1^2 appears to arise due to a transition from a doublet, but of a different symmetry. This could be a Γ_6 doublet. However, in such case, in addition to transitions corresponding to difference of effective g-tensors, also PL lines described by the sum of these parameters should be present. This is not observed in the experiment. Another possibility would be that the hot line originates from a doublet split off from the quadruplet due to the lower symmetry component, a situation similar to that in the ground state, as concluded from analysis of lines L_2^1 and L_3^1.

B. Consequences for the microscopic model of the Er-1 center

Although the microscopic symmetry of the Er-1 center is determined to be orthorhombic I (C_{2v}), we have seen that lines L_2^1 and L_3^1 can be interpreted as arising from a split quadruplet. This could indicate that orthorhombic I distortion of the T_d crystal field is small. It is also consistent with the fact that transition probabilities follow rules of cubic symmetry. Assuming this situation to be true, we can try to place the Er-1 center on the LLW diagram given in Fig. 4. Inspection of this figure shows that the ground state is either Γ_7, for $-1 \leqslant x \leqslant -0.46$, or Γ_6, for $-0.46 \leqslant x \leqslant 0.58$ with W positive. On the other hand, the lowest level of the excited state is a doublet of either $\Gamma_6^{(1)}$, for $-0.57 \leqslant x \leqslant 0.65$, or Γ_7 symmetry, for $0.65 \leqslant x \leqslant 1$. Now, taking into account splitting of PL lines at low temperature and assuming that lines L_2^1, L_3^1 arise from a split quadruplet, the best fit to the experimental data was obtained for three x values: -0.55, -0.07, and 0.41, resulting in W values of 2.046 cm^{-1}, 0.476 cm^{-1}, and 0.739 cm^{-1}, respectively. As can be seen from Fig. 4(b), the corresponding sequence of the ground state levels would be Γ_7, Γ_8, Γ_6, $2\Gamma_8$; Γ_6, Γ_8, Γ_7, $2\Gamma_8$; and Γ_6, Γ_8, Γ_8, Γ_7, Γ_8, respectively. Taking into account the symmetry information obtained from the magnetic field induced splitting of PL lines L_1^1, L_2^1, L_3^1, L_4^1 and L_1^2, the situation with $x = 0.41$ and $W = 0.739$ cm^{-1} for $J = 15/2$ emerges as the most plausible one. The x value is positive as expected for a tetrahedral interstitial position. It is very close to that for the cubic center observed in implanted Si.[14,19] The x-value of the $J = 15/2$ state obtained in this study differs, however, from that of the tetrahedral interstitial Er center observed in implanted Si, $x = 0.35$.[14,19] The discrepancy may be due to the fact that we deal with low-temperature grown silicon, which might have slightly different properties from the Czochralski grown material typically used for implantation. On the other hand, it should be stressed that our analysis bases on the assumption that the C_{2v}-symmetry crystal field can be treated as a small distortion of cubic symmetry, which need not be the case. In fact, the strong anisotropy of the g-tensors indicates rather that the cubic and orthorhombic crystal field potentials may be comparable.

For a cubic symmetry center, x and W values of the $J = 13/2$ state can be determined from these of the $J = 15/2$. In the present case, we should also take into account the Zeeman splitting of the hot line. While this is consistent with a doublet-to-doublet transition, no transitions due to sum of the relevant effective g-tensor values are observed. This indicates the upper state to be arising from a splitting of the quadruplet (in analogy the ground state splitting responsible for lines L_2^1 and L_3^1) rather than a Γ_7 doublet. The possible position of $J = 13/2$ multiplet of the Er-1 center on the LLW diagram is also indicated in Fig. 4.

Finally, we would like to comment on the possible microscopic model of the Er-1 center. This issue is of fundamental importance, as the Er-1 center takes a prominent position of the only Er-related optically active center which can be preferentially generated in crystalline Si. Since the observed splitting is consistent with that which can be expected for an isolated Er^{3+} ion, we can assume that only one Er ion is involved in the structure of Er-1. Also preferential formation of a single configuration is easier to envisage for a center containing one rather than multiple Er ions. The estimated x value of the ground state is positive as expected for a tetrahedral interstitial. This site was predicted from total energy calculations as the most stable configuration of Er^{3+} ion in the crystalline silicon host.[18] Also, channeling studies identified a T_d interstitial site as the preferred location of Er^{3+} ions implanted into Si.[16] Taking into account all the available information, we propose to identify the Er-1 center with an Er^{3+} ion occupying a slightly distorted T_d interstitial site [see Fig. 9(a)].

From analysis of the Zeeman effect we were able to determine the orthorhombic I symmetry of the Er-1 center. The origin of the C_{2v} symmetry distortion is not clear, yet. This relatively high symmetry type is easily realized for defects in crystalline silicon by lifting equivalence of two mutually perpendicular {011} mirror planes. Among other possibilities, it can be achieved by a minor distortion of a T_d site along a $\langle 100 \rangle$ direction, or by a symmetric (with respect to the $\langle 100 \rangle$ axis) incorporation of impurities in one of the planes (see, e.g., microscopic models of negatively charged vacancy

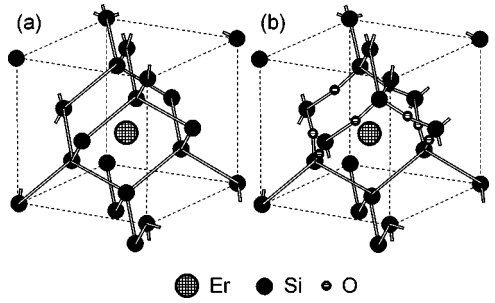

FIG. 9. The possible microscopic structure of the Er-1 center: (a) tetrahedral interstitial Er^{3+} ion with the C_{2v} symmetry obtained by a small distortion along the ⟨100⟩ direction; (b) tetrahedral interstitial Er^{3+} ion-oxygen cluster. The C_{2v} symmetry lowering can be obtained by lattice distortion or by details of oxygen incorporation.

center,[34] substitutional transition metal atoms,[35] thermal donor[36]).

Unfortunately, in contrast to EPR or electron-nuclear double resonance (ENDOR) measurements, no insights on chemical identity or lattice location of ligand atoms can be derived from the present study. We therefore have to rely on the information gathered so far on optical activity of Er in Si. The most prominent conclusion here is that oxygen (as well as other electronegative elements) enhances emission of Si:Er, the effect being optimal for oxygen-to-erbium doping ratio of approximately 10:1. Also EXAFS investigations[15] revealed the presence of six oxygen atoms in the direct surrounding of optically active Er in Czochralski-grown Si. These findings are consistent with results obtained in this study: while no oxygen was intentionally introduced during the SMBE growth process of the multilayer structures used for Zeeman measurements, secondary ion mass spectroscopy (SIMS) analysis shows a clear increase of O concentration ($[O]=1.5\div2\times10^{19}$ cm^{-3}) in the structure when compared to the substrate.[37] Therefore, based on published reports and on the structural information available for the samples used in this project, we propose that the Er-1 center comprises at least 8 oxygen atoms in the direct surrounding of a single Er atom at a high symmetry site. A possible atomic model of such a center is depicted in Fig. 9(b). In this case oxygen atoms have been placed at the usual puckered bonded positions releasing strain on the 4 Si nearest neighbors of the Er. While formation of such a large oxygen complex of specific symmetry might appear not likely at the first glance, we point out that the orthorhombic-*I* C_{2v} symmetry is characteristic for silicon thermal donors formed by oxygen aggregation.[38] Note that the sample growth temperature allows thermal donor formation and Er could enhance oxygen aggregation. On the other hand, the Er-1 center is formed during annealing at 800 °C, at which temperature the thermal donors are found to convert into electrically nonactive aggregates.[39] Unfortunately, owing to the particular *g*-tensor of the ground state, no EPR or ENDOR measurements are possible for the Er-1 center, and no insight into the chemical identity or lattice location of ligand atoms can be derived by these techniques. Therefore the issue of oxygen incorporation in the microstructure of the Er-1 center cannot be concluded at this stage, and will require further investigations.

VI. SUMMARY AND CONCLUSIONS

We present results of a magneto-optical study of multinanolayer Si/Si:Er structures grown by the SMBE technique. We show that the presence of Si spacer regions considerably increases emission intensity when compared to single layers. The PL from annealed multinanolayer structures is dominated by emission from the particular center, the Er-1 center, which is then preferentially formed. The PL spectrum of this center is characterized by ultra narrow homogeneous lines. Based on analysis of the magnetic field induced, angular dependent splitting of the PL lines, we identify the orthorhombic-*I* symmetry of the Er-1 center and give *g*-tensors for several lower-lying levels of the $^4I_{15/2}$ ground and the lowest excited $^4I_{13/2}$ state multiplets. In particular, we identify the original Γ_6 and Γ_7 characters for the lowest crystal-field split levels of the ground and the excited states, respectively. Based on this analysis, we propose that the microscopic structure of the Er-1 center comprises a single Er^{3+} ion at a distorted interstitial T_d site with multiple oxygen atoms in its direct vicinity.

ACKNOWLEDGMENTS

The work was financially supported by the *Nederlandse Organisatie voor Wetenschappelijk Onderzoek* (NWO), and the *European Research Office* (ERO). The authors are grateful to Dr. H. Vrielinck for useful discussions.

[1] S. S. Iyer and Y.-H. Xie, Science **260**, 40 (1993).
[2] S. Schmitt-Rink, C. M. Varma, and A. F. J. Levi, Phys. Rev. Lett. **66**, 2782 (1991).
[3] A. Polman, J. Appl. Phys. **82**, 1 (1997).
[4] J. Palm, F. Gan, B. Zheng, J. Michel, and L. C. Kimerling, Phys. Rev. B **54**, 17603 (1996).
[5] Wai Lek Ng, M. P. Temple, P. A. Childs, F. Wellhofer, and K. P. Homewood, Appl. Phys. Lett. **75**, 97 (1999).
[6] S. Coffa, G. Franzo, and F. Priolo, Mater. Res. Bull. **23**, 25 (1998).
[7] W. Jantsch, S. Lanzerstorfer, M. Stepikhova, H. Preier, and L. Palmetshofer, Solid State Phenom. **69-70**, 53 (1999).
[8] R. S. Smith, H. D. Muller, H. Ennen, P. Wennekers, and M. Maier, Appl. Phys. Lett. **50**, 49 (1987).
[9] K. Thonke, H. U. Hermann, and J. Schneider, J. Phys. C **21**, 5881 (1988).
[10] H. Ennen, J. Wagner, H. D. Muller, and R. S. Smith, J. Appl. Phys. **61**, 4877 (1987).
[11] K. Takahei, A. Taguchi, Y. Horikoshi, and J. Nakata, J. Appl. Phys. **76**, 4332 (1994).
[12] T. Ishiyama, E. Katayama, K. Murakami, K. Takahei, and A. Taguchi, J. Appl. Phys. **84**, 6782 (1998).

[13] D. Haase, A. Dornen, K. Takahei, and A. Taguchi, Mater. Res. Soc. Symp. Proc. **422**, 179 (1996).
[14] H. Przybylinska, W. Jantsch, Y. Suprun-Belevitch, M. Stepikhova, L. Palmetshofer, G. Hendorfer, A. Kozanecki, R. J. Wilson, and B. J. Sealy, Phys. Rev. B **54**, 2532 (1996).
[15] D. L. Adler, D. C. Jacobson, D. J. Eaglesham, M. A. Marcus, J. L. Benton, and J. M. Poate, Appl. Phys. Lett. **61**, 2181 (1992).
[16] U. Wahl, A. Vantomme, J. De Wachter, R. Moons, G. Langouche, J. G. Marques *et al.*, Phys. Rev. Lett. **79**, 2069 (1997).
[17] M. Needels, M. Schluter, and M. Lannoo, Phys. Rev. B **47**, 15 533 (1993).
[18] A. G. Raffa and P. Ballone, Phys. Rev. B **65**, 121309 (2002).
[19] J. D. Carey, R. C. Barklie, J. F. Donegan, F. Priolo, G. Franzo, and S. Coffa, Phys. Rev. B **59**, 2773 (1999).
[20] W. Jantsch, S. Lanzerstorfer, L. Palmetshofer, M. Stepikhova, and H. Preier, J. Lumin. **80**, 9 (1999).
[21] N. Q. Vinh, H. Przybylińska, Z. F. Krasil'nik, and T. Gregorkiewicz, Phys. Rev. Lett. **90**, 066401 (2003).
[22] B. A. Andreev *et al.*, J. Cryst. Growth **201/202**, 534 (1999); M. V. Stepikhova *et al.*, Thin Solid Films **369**, 426 (2000).
[23] V. P. Kuznetsov, A. Y. Andreev, O. A. Kuznetsov, L. E. Nikolaeva, T. M. Sotova, and N. V. Gudkova, Phys. Status Solidi A **127**, 371 (1991).
[24] A. Abragam and B. Bleaney, *Electron Paramagnetic Resonance of Transition Ions* (Clarendon, Oxford, 1970).
[25] K. R. Lea, M. J. M. Leask, and W. P. Wolf, J. Phys. Chem. Solids **23**, 1381 (1962).
[26] G. H. Dieke, *Spectra and Energy Levels of Rare Earth Ions in Crystals* (Wiley, New York, 1968).
[27] J. D. Kingsley and M. Aven, Phys. Rev. **155**, 235 (1967).
[28] B. Bleaney, Proc. Phys. Soc. London **73**, 939 (1959).
[29] G. F. Koster, J. O. Dimmock, R. G. Wheeler, and H. Statz, *Properties of the Thirty-Two Point Groups* (MIT Press, Cambridge, 1963).
[30] U. Ranon and W. Low, Phys. Rev. **132**, 1609 (1963).
[31] M. J. Weber and R. W. Bierig, Phys. Rev. **134**, A1492 (1964).
[32] R. K. Watts and W. C. Holton, Phys. Rev. **173**, 417 (1968).
[33] B. L. Crowder, R. S. Title, and G. D. Pettit, Phys. Rev. **181**, 567 (1969).
[34] M. Sprenger, S. H. Muller, E. G. Sieverts, and C. A. J. Ammerlaan, Phys. Rev. B **35**, 1566 (1987).
[35] G. D. Watkins, M. Kleverman, A. Thilderkvist, and H. G. Grimmeiss, Phys. Rev. Lett. **67**, 1149 (1991).
[36] T. Gregorkiewicz, H. H. P. Th. Bekman, and C. A. J. Ammerlaan, Phys. Rev. B **38**, 3998 (1988).
[37] F. W. Widdershoven (private communication).
[38] T. Gregorkiewicz, H. H. P. Th. Bekman, and C. A. J. Ammerlaan, Phys. Rev. B **41**, 12 628 (1990).
[39] P. Wagner and J. Hage, Appl. Phys. A: Solids Surf. **49**, 123 (1989).